Experimental and finite element analysis of PPF controller effectiveness in composite beam vibration suppression

Andrzej Mitura[a,*], Jaroslaw Gawryluk[a]

[a] Lublin University of Technology, Faculty of Mechanical Engineering, Department of Applied Mechanics, ul. Nadbystrzycka 36, 20-618 Lublin, Poland

Highlights

- Own procedures were added to the FE model to extend the MFC actuator model.
- The influence of the MFC hysteresis on the control effectiveness was tested numerically.
- The obtained numerical results were experimentally verified.
- The PPF controller can be applied to protect the beam against resonance vibrations.

Abstract

In this paper the problem of vibration reduction is considered. Generally, mechanical vibrations occurring during the operation of a system are undesirable and may have a negative effect on its reliability. A finite element model of a single active blade is developed using the Abaqus software. This structure consists of a multi-layer glass-epoxy composite beam with an embedded macro fiber composite (MFC) piezoelectric actuator. For vibration control the use of a positive position feedback (PPF) controller is proposed. To include the PPF controller in the Abaqus software, a special subroutine is created. The developed control algorithm code makes it possible to solve an additional differential equation by the fourth order Runge-Kutta method. A numerical dynamic analysis is performed by the implicit procedure. The beam responses with and without controller activation are compared. The control subsystem model also includes the hysteresis phenomenon of the piezoelectric actuator. Numerical findings regarding the PPF controller's effectiveness are verified experimentally.

Keywords

finite element method, positive position feedback control, composite structures, hysteresis phenomenon, macro fiber composite.

1. Introduction

Composites are modern materials that have taken on an immense significance in the 21st century. Although their applications can be found everywhere, the most interesting are those in specialized devices. For example, helicopter rotor or wind turbines blades are made of composite materials. Rotating elements are subjected to different loads, e.g. those induced by variable wind speed [19]. As a result, mechanical vibrations of the blades may be produced. Additional oscillations may affect the operating condition and reliability of a system. High amplitude-resonance vibrations can cause sudden structural damage. These undesirable resonance regions can be detected by an experimental modal analysis. Such modal research for small aircraft is presented in [10]. The smaller oscillations with long-lasting are also dangerous, because the fatigue effect can be observed. For example, a fatigue problem analysis for a composite wind turbine blade is shown in [5]. The reliability of modern systems requires monitoring of vibration level and its reduction under certain conditions. In paper [2] has been shown that the vibrations reduction can significantly reduce the dynamic loads. The obtained dynamic forces and moments were lower when the control was activated. The above arguments confirm that the blades dynamics should be controlled to avoid undesirable vibrations. The literature review shows a large number of dynamic and control studies on such structures. In [18] the results of an experimental modal analysis for a real main rotor blade were presented. Natural frequencies and vibration modes were specified for one blade from the IS-2 helicopter. The knowledge of basic dynamic parameters is insufficient to fully evaluate the system dynamics. However, studying a helicopter in flight is complicated and expensive. Therefore, scientists often study the rotor with blades or single blade models. The scaled rotors with 2, 3 or 4 blades were investigated in [17]. The authors of the study developed an experimental stand with the most important elements of the mechanism included. Consequently, it was possible to vary the pitch angle of the blades during rotor rotation. This way of modelling made it possible to study the aerodynamic properties of the model. In [14] a more simplified model of the helicopter rotor was presented. In this model three blades were clamped to the rotor hub. In effect, only constant pitch angle setting during hub rotation was possible. The study evaluated the influence of the centrifugal force in natural frequencies. The authors used piezoelectric actuators attached to the surface of the composite blades. Although in the aforementioned study the actuators were used as excitation generators, they can also be used to control vibration. This application for piezoelectric actuators was described in [22]. Special piezoelectric patches were embedded inside the blade structure so that they generated strains in a direc-

(*) Corresponding author.
E-mail addresses: A. Mitura (ORCID: 0000-0002-6749-8232): a.mitura@pollub.pl, J. Gawryluk (ORCID: 0000-0001-5075-5207): j.gawryluk@pollub.pl

tion deflected at ±45° to the spanwise axis. For such piezoelectric actuator orientation it is possible to obtain the maximum blade torsion control. The study has shown the effect of active twist control on vibration and noise reduction. Piezoelectric actuators of this type were also tested in other studies. Gawryluk et al. developed a finite element model of a blade with a piezoelectric element [7]. The modelling was based on previous studies [14] in which static and eigenvalue problems were considered. New simulations were made in time domain using an implicit solver. The role of the MFC actuator was limited to that of an excitation generator. In [6] the role of the MFC actuator was extended to vibration control. Experimental and numerical resonance characteristics of the system with the proportional controller were compared. The results showed significant discrepancies in the location of resonance peaks. It was found that the desired control load and the actuator load are different. A new approach was proposed, where both loads (desired and applied) were related by a first order inertial term. The study showed that the correct mapping of system dynamics had to consider the properties of a piezoelectric element. In [13] the response of a piezoelectric actuator on changing its voltage using step or triangular signals was investigated. This type of testing allowed for the visualization of main nonlinear properties of PZT elements. The results revealed the presence of creep and hysteresis. The authors proposed using the fractional order Maxwell resistive capacitor model for modelling these effects. Kedra and Rucka suggested that piezoelectric hysteresis could be described using different models, e.g. the Preisach model, the Duhem model, the Backlash model, the Prandtl-Ishlinski model, the Bouc-Wen model [9]. However, they decided to use the Bouc-Wen model and described the methodology for identifying its parameters. The Bouc-Wen model and its modifications were employed in many studies, for example: the identification method of its constants from experimental data [4] and investigation of the asymmetry aspect of the hysteresis characteristic [12]. In paper [15] it was shown that the discrepancy between desired control load and piezoelectric patch load may result not only from the actuator's properties but also from the properties of its amplifier. In a mathematical model, the Bouc-Wen hysteresis model and the first order inertial term were applied. Results showed that hysteresis may affect the effectiveness of a selected control algorithm. For a rotating cantilever beam, different controllers can be used. In [8] macro fiber composite actuators and sensors were used for vibration control in a rotating blade. Vibration reduction was ensured via the use of a positive position feedback controller. Obtained characteristics indicated the possibility of vibration control in a specific frequency range. Generally, a single PPF controller can be used to control one vibration mode. However, the use of several PPF controllers simultaneously leads to multimodal vibration suppression [11]. This kind of controller outside the zone of favorable control can generate unwanted vibration. This can be avoided by selecting optimal controller parameters, as shown in [3]. It is also possible to use other control algorithms. Vadiraja and Sahasrabudhe applied the optimal linear quadratic Gaussian controller to vibration control of rotating thin-walled beams [21]. Optimal control load depends on the estimated state and control gain obtained from the Riccati equation. Generally, the procedure for voltage determination is more complex than that for PPF control. For the purpose of this study, PPF control was selected, owing to the simplicity of the algorithm and the possibility of combining optimal single controllers to reduce many vibration resonances.

This paper is a continuation of the research on the development of an active rotor blade. Results of previous studies were published in a series of research papers [6, 7, 14]. However, these studies did not consider the influence of MFC actuator hysteresis on vibration control efficiency. In the finite element analysis described in this paper, two dependencies on the desired load and that generated by a piezoelectric actuator are compared. The first order inertial term and the Bouc-Wen model are used. The consideration of these factors requires the creation of an appropriate subroutine for subsequent integration steps, using the Abaqus software. The first attempts were made with the use of Euler's method [6]. In this study, the fourth order Runge-Kutta method is applied because Euler's method was found to be unsatisfactory. The numerical analysis has shown that hysteresis can affect the PPF controller's efficiency. In addition, the trends obtained numerically were experimentally verified. This paper consists of the following sections: FE model of an active beam, numerical results, experimental findings, and conclusions.

2. FE model of an active beam

In this study a simplified model is considered, with one blade taken from the rotor and mounted on an electrodynamic shaker TIRA GmbH TV501-01. The applied experimental setup is shown in Figure 1. The composite beam was made of unidirectional glass-epoxy prepreg TVR380M12/26%R-Glass using autoclave technique. The structure had six layers with the fiber orientation $[\pm 45/90]_S$. The beam geometry was described by a total length of 350 mm (beam length after clamping was 316 mm), a width of 34 mm, and a thickness of 1.8 mm. More details about, e.g. strength parameters, can be found in [14]. Vibration of the composite beam was generated with a shaker. To control the beam vibration level, an actuator and a sensor were applied. Owing to its high flexibility, the macro fiber composite actuator was used to this end. This is a special type of actuator produced by Smart Materials Corp., wherein the piezoelectric material fibers are embedded in the resin and between the electrodes. With an appropriate configuration of the electrodes, it is possible to obtain the d_{31} or d_{33} effect [20]. Since higher efficiency can be obtained using an actuator with the d_{33} piezoelectric effect, such MFC element (M-8528-P1) was used. The symbol 8528 defines an active area of the actuator. It is a rectangle with the sides 85 mm and 28 mm. The MFC patch was attached near the clamp, and the distance between the handle and the beginning of the active area was about 16 mm. This location was selected based on the recommendation for cantilever structures given in [16]. Real-time control requires the use of a controller. The proposed device is based on a digital signal processor (DSP). The desired control algorithm can be defined in a DSP controller code. Generally, the controller output has an electric signal with a maximum voltage of about ±10 volts. The MFC actuator must, however, be powered with high voltage. The d_{33} actuators can be supplied with a voltage ranging from 500 V to 1500 V. Therefore, a high voltage amplifier was used. In this way, the voltage from the controller could be increased by two hundred times.

For the proposed system, a finite element model was developed in the Abaqus software. Based on previous research [7], the composite beam was modelled using SC8R continuum shell elements and the layup-ply technique was used to make its individual layers. The piezoelectric actuator was modelled using C3D20RE solid elements that are associated with piezoelectricity properties. Generally, the MFC actuator has a very complex structure. A simplified description of the piezoelectric element was applied. For example, instead of real many pairs of electrodes, the model had only one such pair. Basic assumptions of the simplifications applied were presented in [7], while the reduced parameters of the MFC model were taken from [6]. Both parts – the beam and the actuator, were connected by TIE interactions [1]. Kinematic excitation was generated using mechanical boundary conditions. The points on one end of the beam could only move vertically by the function:

$$z_{\text{shaker}} = z_0 \sin \omega t \qquad (1)$$

where z_0, ω are the amplitude and the frequency of excitation, respectively.

The DSP controller modelling required the use of an UAMP subroutine. Figure 2 shows the diagram illustrating the relationship between the subroutine object and the rest of the model. Displacement of a selected beam point was used as an input. The developed own code was used to calculate a subroutine output. The output was a volt-
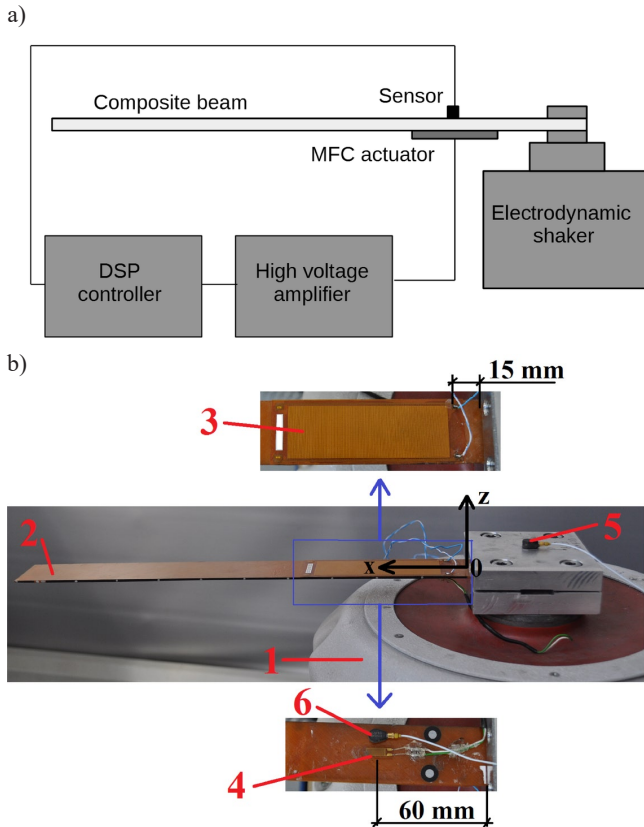
Fig. 1. Scheme of the experimental setup (a) and images of an active beam (b) and a control subsystem (c)1- electrodynamic shaker TIRA GmbH TV501-01, 2- composite beam, 3- MFC M-8528-P1 patch, 4- strain gauge control sensor, 5- accelerometer Piezotronics PCB352A24 for shaker control, 6- additional accelerometer Piezotronics PCB352A24, 7- DSP controller, 8- High Voltage Amplifier Smart Materials HVA1500/50-4, 9- external D/A signal converter.

age for powering the piezoelectric actuator. This signal was assigned the properties of electrical boundary condition of the MFC element. In this study, the basic code version describes the positive position feedback control. This is a so-called ideal control case where the desired and realized MFC voltages are proportional. Code modifications took into account additional first-order differential equations. These equations describe specified properties of the actuator. Consequently, the desired and the realized voltage can be different because the hysteresis phenomenon is included. More details are provided in the next section of this paper, where selected simulation results are presented.

3. Numerical results

This section presents selected results of the numerical simulations. In the numerical calculations, the kinematic excitation (1) with an amplitude of $z_0 = 1$ mm was applied. The frequency was changed from 7.5 to 10.5 Hz. It was the first bending resonance zone. Obtained time
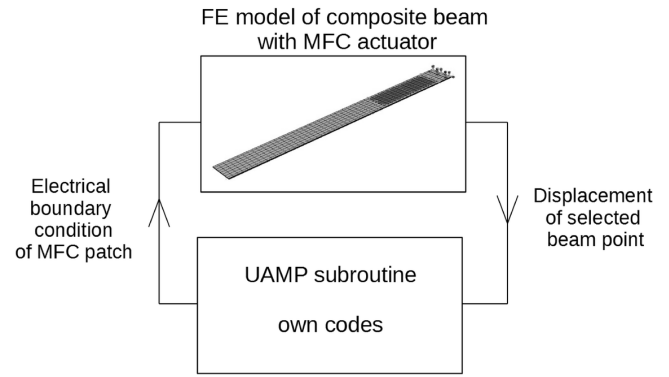

Fig. 2. Scheme of the control concept in Abaqus

series were used to determine the characteristics of amplitude vibration via excitation frequency. Vertical displacement of two points on the beam, z_{beam}, was measured. The first point corresponded to the sensor location (x=60 mm). A signal from this point was necessary for vibration control and we called it Abaqus sensor signal. The free end of the beam (x=316 mm) was the other point. By knowing its displacement it is possible to determine maximum beam vibration. The absolute vertical displacement z_{beam} and the shaker armature motion z_{shaker} were used to determine beam deflection, its relative motion w being:

$$w = z_{beam} - z_{shaker} \qquad (2)$$

Obtained results were divided into three cases: for a system without control, for a system with ideal control, and for a system with non-ideal control.

3.1. System dynamics without control

This subsection is devoted to an analysis of the dynamics of a system without control. In this case, the controller was deactivated. Beam vibration was induced in two ways. In the first variant, beam motion was excited kinematically by an electrodynamic shaker. In the other variant, the embedded MFC actuator served as a generator of beam vibration. A comparison of the obtained resonance curves is shown in Figure 3. It can be observed that the excitation from the shaker with an amplitude of $z_0 = 1$ mm produced a low-amplitude vibration of the beam. Curves similar to those obtained for a linear oscillator can be observed (Fig. 3a). The observed maximum vibration amplitude is about 14% of the beam length. For the first bending mode, the resonance frequency is $\omega_0 \approx 57.8$ rad/s (9.2 Hz).

In the second tested variant, the beam vibration was only induced by the MFC actuator. The voltage on its electrodes, U_{MFC}, was changed periodically with an amplitude of 500 V. The results demonstrate that it is possible to obtain the maximum vibration of about 55 mm. This is very good information because it means that the piezoelectric actuator has enough power to suppress beam vibration. This assumption is based on the fact that the maximum amplitude in the second variant (Fig. 3b) is higher than in the first variant (Fig. 3a). Therefore, the MFC patch load can be higher than the impact of kinematic excitation and can thus effectively suppress beam vibration.

3.2. System dynamics with ideal control

The selected control algorithm was tested via numerical simulations. Previous studies indicate that for cantilever beams, positive position feedback control is recommended [11]. The practical implementation of this type of control requires writing differential equation in the DSP controller code. This control equation has the following form:

$$\ddot{U}_{control} + \omega_{control}^2 U_{control} + 2n\dot{U}_{control} = \gamma_1 w_{sensor} \qquad (3)$$
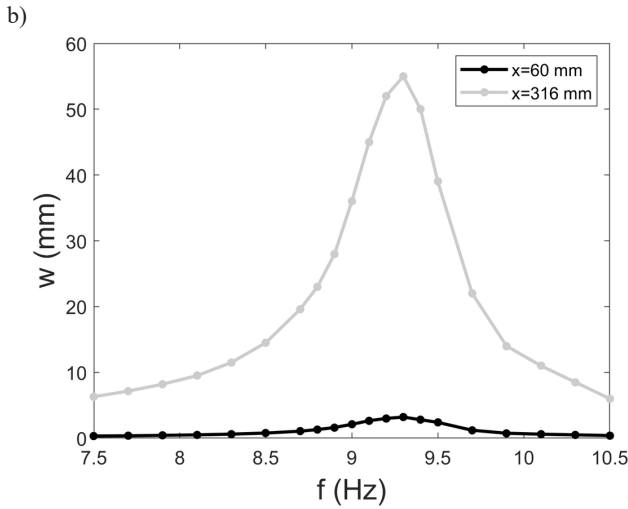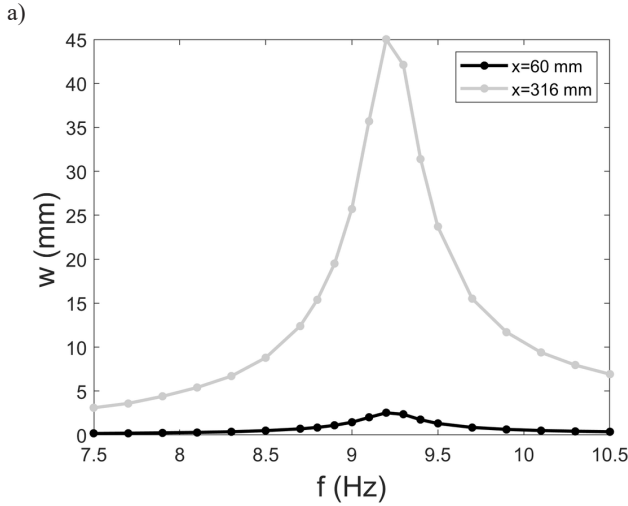
a)

b)

Fig. 3. Resonance characteristics of the systems without control and with excitation from: shaker (a) and MFC element (b)

where $U_{control}$ is the calculated control signal, $\omega_{control}$ and n are the control parameters, and w_{sensor}, γ_1 are the signal from the sensor and input gain, respectively. Based on the desired control signal, the voltage applied to the MFC element U_{MFC} is calculated as:

$$U_{MFC} = \gamma_2 U_{control} \qquad (4)$$

where the gain γ_2 includes high voltage amplifier gain and control gain. It is assumed that $\gamma_2 = 1000$. It is an idealized control method where both signals U_{MFC} and $U_{control}$ are proportional (Fig. 4). In a real system there may occur many additional factors that are not considered in this description.

For the controller in question, a subroutine code was developed. The starting point for developing this code was a study [6], where the codes were written for the P and PD controllers with the first order inertial term. For integration, the Euler's method was used. The first attempts to program the PPF controller were made by this method. However, the Euler's method did not yield satisfactory results. Therefore, a more complicated notation with the fourth order Runge-Kutta method was employed. The index i is used in the code. This parameter provides information about a moment in time, where i is the considered time, i-1 is the previous moment ($t_{i-1} = t_i - \Delta t$).

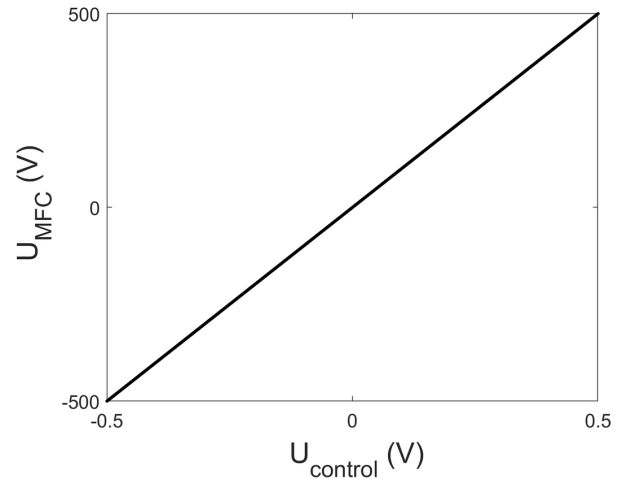An own code based on the following dependencies was written in the UAMP subroutine:

Fig. 4. Control signal versus supply voltage of the MFC patch

$$K_1 = V_{control,i-1}$$

$$M_1 = -\omega_{control}^2 U_{control,i-1} - 2nV_{control,i-1} + \gamma_1 w_{sensor,i-1}$$

$$K_2 = V_{control,i-1} + \frac{1}{2}\Delta t M_1$$

$$M_2 = -\omega_{control}^2\left(U_{control,i-1} + \frac{1}{2}\Delta t K_1\right) - 2n\left(V_{control,i-1} + \frac{1}{2}\Delta t M_1\right) + \gamma_1 w_{sensor,i-1}$$

$$K_3 = V_{control,i-1} + \frac{1}{2}\Delta t M_2$$

$$M_3 = -\omega_{control}^2\left(U_{control,i-1} + \frac{1}{2}\Delta t K_2\right) - 2n\left(V_{control,i-1} + \frac{1}{2}\Delta t M_2\right) + \gamma_1 w_{sensor,i-1}$$

$$K_4 = V_{control,i-1} + \Delta t M_3$$

$$M_4 = -\omega_{control}^2\left(U_{control,i-1} + \Delta t K_3\right) - 2n\left(V_{control,i-1} + \Delta t M_3\right) + \gamma_1 w_{sensor,i-1}$$

$$U_{control,i} = U_{control,i-1} + \frac{\Delta t}{6}\left(K_1 + 2K_2 + 2K_3 + K_4\right)$$

$$V_{control,i} = V_{control,i-1} + \frac{\Delta t}{6}\left(M_1 + 2M_2 + 2M_3 + M_4\right)$$

$$U_{MFC,i} = \gamma_2 U_{control,i} \qquad (5a\text{-}5k)$$

where the symbol $V_{control}$ in the code is equivalent to $\dot{U}_{control}$, because leaving the dots could be ambiguous. The designations K_1, K_2, K_3, K_4 and M_1, M_2, M_3, M_4 define the indirect calculations in the RK4 algorithm. They are employed to calculate state variables in a new iteration. K_i and M_i are used to calculate $U_{control}$, $V_{control}$ respectively.

The above procedures (5a-5k) are the same as the code that should be written in the DSP controller. The simulations were performed for the following PPF control parameters: $\gamma_1 = 50000$ s^{-2}, $\gamma_2 = 1000$, $\omega_{control} = 58.12$ rad/s, $n = 2$ rad/s. The controller natural frequency $\omega_{control}$ is related to the so-called dynamic vibration elimination point. The absence of damping (n=0) and the excitation frequency equal to $\omega = \omega_{control}$ ensure that there is no beam vibration (w=0). However, the maximum reduction in vibration at one point ($\omega = \omega_{control}$) results in an undesired increase in the resonances amplitudes of the system with control. In practice, a compromise has to be found. This can be done by selecting an appropriate value of the controller damping n. A comparison of the resonance curves for the system without and with control is shown in Figure 5. The results indicate the possibility of a significant reduction of beam vibration in the resonance zone. An approximately 60% reduction in the maximum beam vibration is observed. This significant decrease in beam vibration is accompanied by a slight increase in the vibration outside

the resonance zone, for the excitation frequency higher than 9.6 Hz or lower than 8.9 Hz.
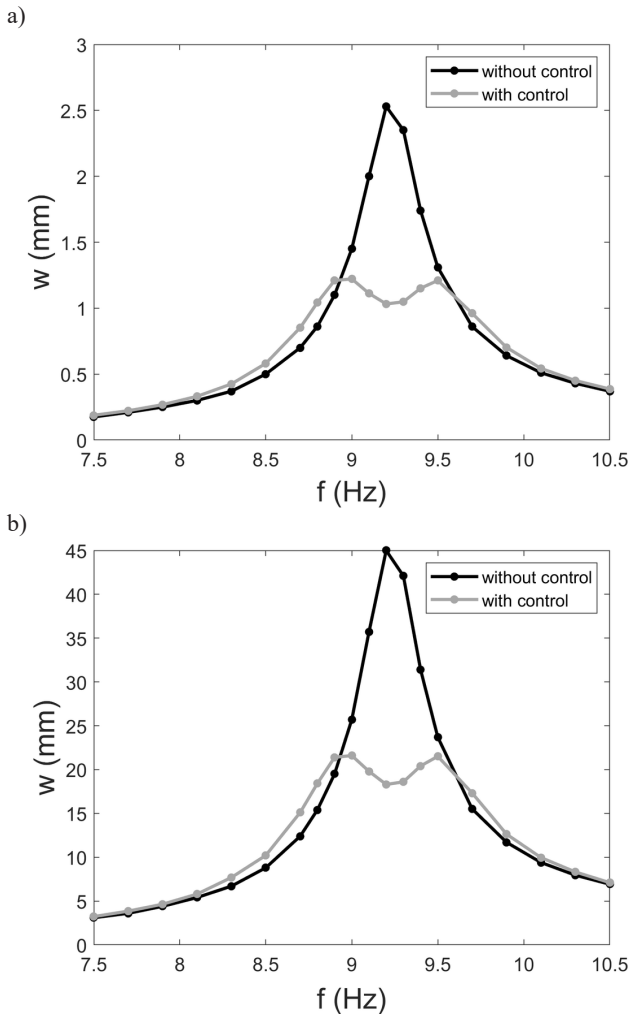
a)

b)

Fig. 5. Comparison of the resonance curves for a system without and with ideal control, and the results of: Abaqus sensor signal (a), free end response (b)
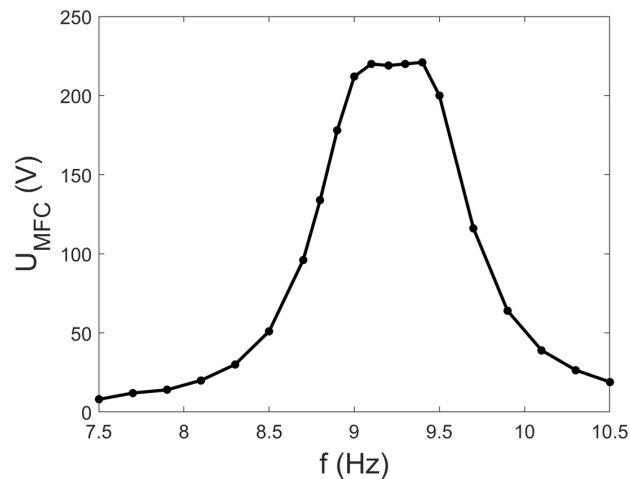

Fig. 6. Resonance curves of the voltage supplied to the MFC actuator

In the simulations, the voltage from the electrical boundary condition U_{MFC} was also measured. As a result, it was possible to determine the extent of the MFC actuator's capability. Generally, the voltage U_{MFC} can range from -500 V to 1500 V. For the selected control algorithm, a symmetric voltage range from -500 V to 500 V is useful. In this study only 45% of this range was used (Fig. 6).

3.3. System dynamics with non-ideal control

In a real control system many additional effects may occur, for example hysteresis. Therefore, the description of the control process was extended. Based on previous studies [6, 15], two variants of modification were introduced. In the first variant, the first- order inertial term was added:

$$\ddot{U}_{control} + \omega^2_{control}U_{control} + 2n\dot{U}_{control} = \gamma_1 w_{sensor} \tag{6a}$$

$$\tau\dot{U}_{MFC} + U_{MFC} = \gamma_2 U_{control} \tag{6b}$$

where τ is the time constant.

In [6] it was argued that Equation (6b) could be used to describe some global properties of a control subsystem. It can be assumed that this may result from, for example, the characteristics of a high-voltage amplifier. On the other hand, in [15] the nonlinear properties of a piezoelectric actuator were emphasized. One way of modelling piezoelectric hysteresis is via using the Bouc-Wen model. In the other variant, the following model was used:

$$\ddot{U}_{control} + \omega^2_{control}U_{control} + 2n\dot{U}_{control} = \gamma_1 w_{sensor} \tag{7a}$$

$$\dot{z} = \alpha\dot{U}_{control} - \beta z\left|\dot{U}_{control}\right| - \delta\dot{U}_{control}\left|z\right| \tag{7b}$$

$$U_{MFC} = \gamma_2 U_{control} - \lambda z \tag{7c}$$

In both of these modifications hysteresis loops can be obtained. Examples of the shapes (Fig. 7) were simulated from (6b) and (7b-c), for the following parameters: $U_{control} = 0.5\sin(2\pi ft)$, $f = 8$ Hz, $\gamma_2 = 1000$, $\tau = 0.0215$ s, $\lambda = 0.2075$, $\alpha = 471.4$, $\beta = 2.38$ V^{-1}, $\delta = 0.0326$ V^{-1}. In the first mechanism based on Equation (6b), an ellipse-shaped loop can be observed (Fig. 7a). In this case the loop size only depends on the time constant τ. In the Bouc-Wen model however, a more complex shape can be obtained (Fig. 7b). In Equation (7c) there are three parameters: α, β, δ, which can change the loop shape. The loop size can be changed by applying a new value of the λ parameter in Equation (7c).

The curves of U_{MFC} versus $U_{control}$ are different than those obtained for ideal control (Fig. 4). An analysis of a system with hysteresis was called as a test with non-ideal control. To perform this test, the UAMP subroutine code had to be modified.

For the first variant, Equations (6a-b), the UAMP subroutine code includes the following dependencies:

$$K_1 = V_{control,i-1}$$

$$M_1 = -\omega^2_{control}U_{control,i-1} - 2nV_{control,i-1} + \gamma_1 w_{sensor,i-1}$$

$$N_1 = \frac{1}{\tau}\left(-U_{MFC,i-1} + \gamma_2 U_{control,i-1}\right)$$

$$K_2 = V_{control,i-1} + \frac{1}{2}\Delta t M_1$$

$$M_2 = -\omega^2_{control}\left(U_{control,i-1} + \frac{1}{2}\Delta t K_1\right) - 2n\left(V_{control,i-1} + \frac{1}{2}\Delta t M_1\right) + \gamma_1 w_{sensor,i-1}$$

$$N_2 = \frac{1}{\tau}\left(-\left(U_{MFC,i-1} + \frac{1}{2}\Delta t N_1\right) + \gamma_2 U_{control,i-1} + \frac{1}{2}\Delta t K_1\right)$$
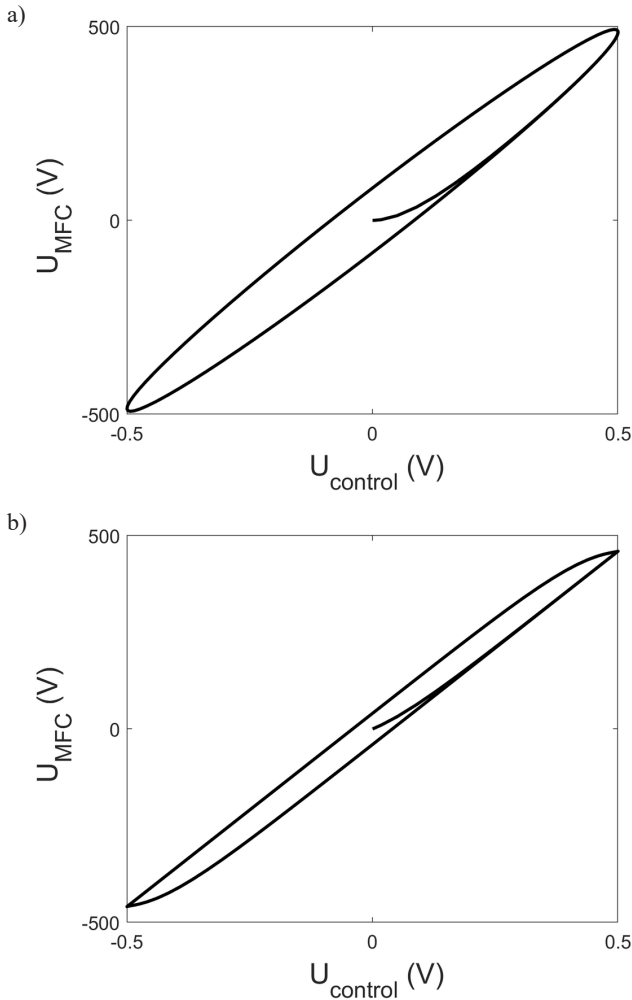
$$K_3 = V_{control,i-1} + \frac{1}{2}\Delta t M_2$$

a)

b)

Fig. 7. Comparison of two hysteresis mechanisms. (a) first order inertial term, (b) Bouc-Wen model

$$M_3 = -\omega_{control}^2\left(U_{control,i-1} + \frac{1}{2}\Delta t K_2\right) - 2n\left(V_{control,i-1} + \frac{1}{2}\Delta t M_2\right) + \gamma_1 w_{sensor,i-1}$$

$$N_3 = \frac{1}{\tau}\left(-\left(U_{MFC,i-1} + \frac{1}{2}\Delta t N_2\right) + \gamma_2 U_{control,i-1} + \frac{1}{2}\Delta t K_2\right)$$

$$K_4 = V_{control,i-1} + \Delta t M_3$$

$$M_4 = -\omega_{control}^2\left(U_{control,i-1} + \Delta t K_3\right) - 2n\left(V_{control,i-1} + \Delta t M_3\right) + \gamma_1 w_{sensor,i-1}$$

$$N_4 = \frac{1}{\tau}\left(-\left(U_{MFC,i-1} + \Delta t N_3\right) + \gamma_2 U_{control,i-1} + \Delta t K_3\right)$$

$$U_{control,i} = U_{control,i-1} + \frac{\Delta t}{6}\left(K_1 + 2K_2 + 2K_3 + K_4\right)$$

$$V_{control,i} = V_{control,i-1} + \frac{\Delta t}{6}\left(M_1 + 2M_2 + 2M_3 + M_4\right)$$

$$U_{MFC,i} = U_{MFC,i-1} + \frac{\Delta t}{6}\left(N_1 + 2N_2 + 2N_3 + N_4\right) \quad (8a-8o)$$

For the second tested variant, Equations (7a-c), the UAMP subroutine code includes other dependencies:

$$K_1 = V_{control,i-1}$$

$$M_1 = -\omega_{control}^2 U_{control,i-1} - 2nV_{control,i-1} + \gamma_1 w_{sensor,i-1}$$

$$N_1 = \alpha V_{control,i-1} - \beta z_{i-1}\left|V_{control,i-1}\right| - \delta V_{control,i-1}\left|z_{i-1}\right|$$

$$K_2 = V_{control,i-1} + \frac{1}{2}\Delta t M_1$$

$$M_2 = -\omega_{control}^2\left(U_{control,i-1} + \frac{1}{2}\Delta t K_1\right) - 2n\left(V_{control,i-1} + \frac{1}{2}\Delta t M_1\right) + \gamma_1 w_{sensor,i-1}$$

$$N_2 = \alpha\left(V_{control,i-1} + \frac{1}{2}\Delta t M_1\right) - \beta\left(z_{i-1} + \frac{1}{2}\Delta t N_1\right)\left|V_{control,i-1} + \frac{1}{2}\Delta t M_1\right| - \delta\left(V_{control,i-1} + \frac{1}{2}\Delta t M_1\right)\left|z_{i-1} + \frac{1}{2}\Delta t N_1\right|$$

$$K_3 = V_{control,i-1} + \frac{1}{2}\Delta t M_2$$

$$M_3 = -\omega_{control}^2\left(U_{control,i-1} + \frac{1}{2}\Delta t K_2\right) - 2n\left(V_{control,i-1} + \frac{1}{2}\Delta t M_2\right) + \gamma_1 w_{sensor,i-1}$$

$$N_3 = \alpha\left(V_{control,i-1} + \frac{1}{2}\Delta t M_2\right) - \beta\left(z_{i-1} + \frac{1}{2}\Delta t N_2\right)\left|V_{control,i-1} + \frac{1}{2}\Delta t M_2\right| - \delta\left(V_{control,i-1} + \frac{1}{2}\Delta t M_2\right)\left|z_{i-1} + \frac{1}{2}\Delta t N_2\right|$$

$$K_4 = V_{control,i-1} + \Delta t M_3$$

$$M_4 = -\omega_{control}^2\left(U_{control,i-1} + \Delta t K_3\right) - 2n\left(V_{control,i-1} + \Delta t M_3\right) + \gamma_1 w_{sensor,i-1}$$

$$N_4 = \alpha\left(V_{control,i-1} + \Delta t M_3\right) - \beta\left(z_{i-1} + \Delta t N_3\right)\left|V_{control,i-1} + \Delta t M_3\right| - \delta\left(V_{control,i-1} + \Delta t M_3\right)\left|z_{i-1} + \Delta t N_3\right|$$

$$U_{control,i} = U_{control,i-1} + \frac{\Delta t}{6}\left(K_1 + 2K_2 + 2K_3 + K_4\right)$$

$$V_{control,i} = V_{control,i-1} + \frac{\Delta t}{6}\left(M_1 + 2M_2 + 2M_3 + M_4\right)$$

$$z_i = z_{i-1} + \frac{\Delta t}{6}\left(N_1 + 2N_2 + 2N_3 + N_4\right)$$

$$U_{MFC,i} = \gamma_2 U_{control,i} - \lambda z_i \quad (9a-9p)$$

Additional designations of the indirect calculations N_1, N_2, N_3, N_4 are given in Equations (8) and (9). They are used to calculate new state variable from the hysteresis differential equation.

Simulations of the non-ideal control system were performed for the following PPF control parameters: $\gamma_1 = 50000\ s^{-2}$, $\gamma_2 = 1000$, $\omega_0 = 58.12$ rad/s, $n = 2$ rad/s and two sets of hysteresis parameters. For the model with the first-order inertial term, the values $\tau = 0.005$ s and $\tau = 0.0215$ s were applied. In the Bouc-Wen model, the only changed values were: $\lambda = 0.2075$ and $\lambda = 0.6225$. Other parameters were constant, i.e. $\alpha = 471.4$, $\beta = 2.38\ V^{-1}$, $\delta = 0.0326\ V^{-1}$.

A comparison of the resonance curves for a system without control and with the first variant of non-ideal control is presented in Figure 8. For a small time constant value of $\tau = 0.005$ s, the characteristic is similar to that obtained for the ideal control system ($\tau = 0$ s). Nevertheless, some differences can be observed. The most significant change induced by the presence of the first-order inertial term is the change in the height of amplitude peaks. The first peak is smaller and the second peak is larger, compared to the system with ideal control. A continuation of this trend is observed for a larger value of the time constant, i.e. $\tau = 0.0215$ s. Now, the first peak is much smaller (and thus cannot be detected) while the second peak is considerably higher. Based on the data, it can be concluded that an increase in the time constant τ significantly changes the beam dynamics. As a result, the control efficiency is reduced.

A similar analysis was performed for the second tested variant of non-ideal control (Fig. 9). For the low Bouc-Wen hysteresis parameter $\lambda = 0.2075$, the characteristics are similar to those obtained for the ideal control system ($\lambda = 0$). A comparison of the resonance peaks reveals that the Bouc-Wen model has a lower first peak and a higher second peak than is the case with the ideal control system. The application of the larger value $\lambda = 0.6225$ changes the amplitude peak height. The first peak cannot be detected and the second peak is much higher. Based on the data, it can be concluded that increase in λ results in lower control efficiency.

The results obtained for the two tested non-ideal control variants indicate similar trends. Generally, the shapes of hysteresis loops are different for the model with the inertial term and the Bouc-Wen model. However, both approaches induce the same qualitative changes,
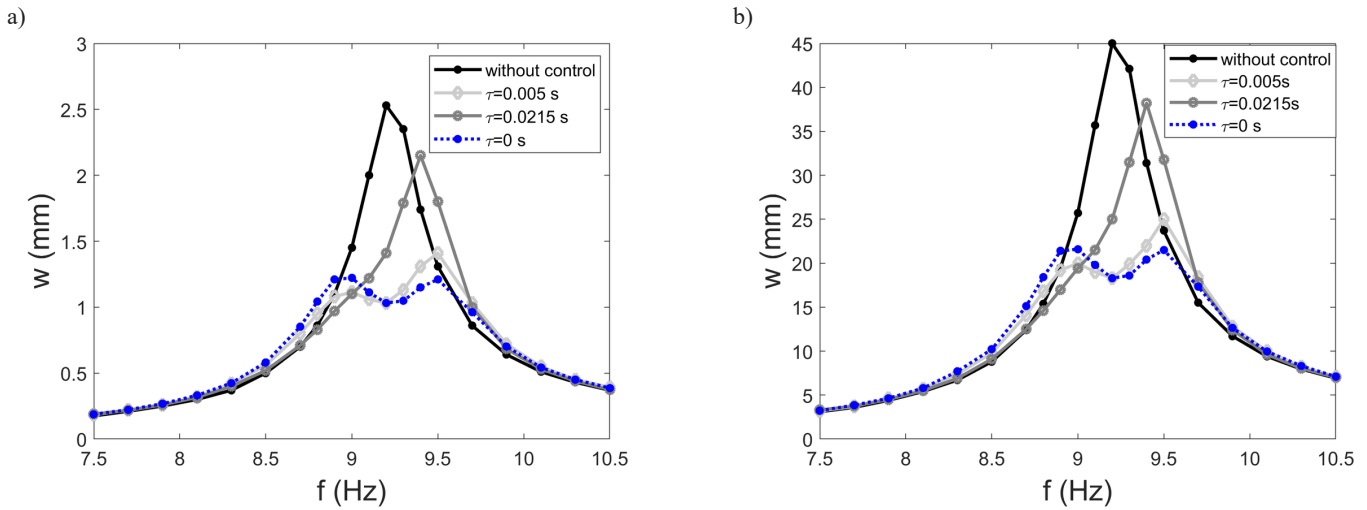
Fig. 8. Comparison of the resonance curves for a system without control and with the first variant of non-ideal control, and the results of: Abaqus sensor signal (a), free end response (b)
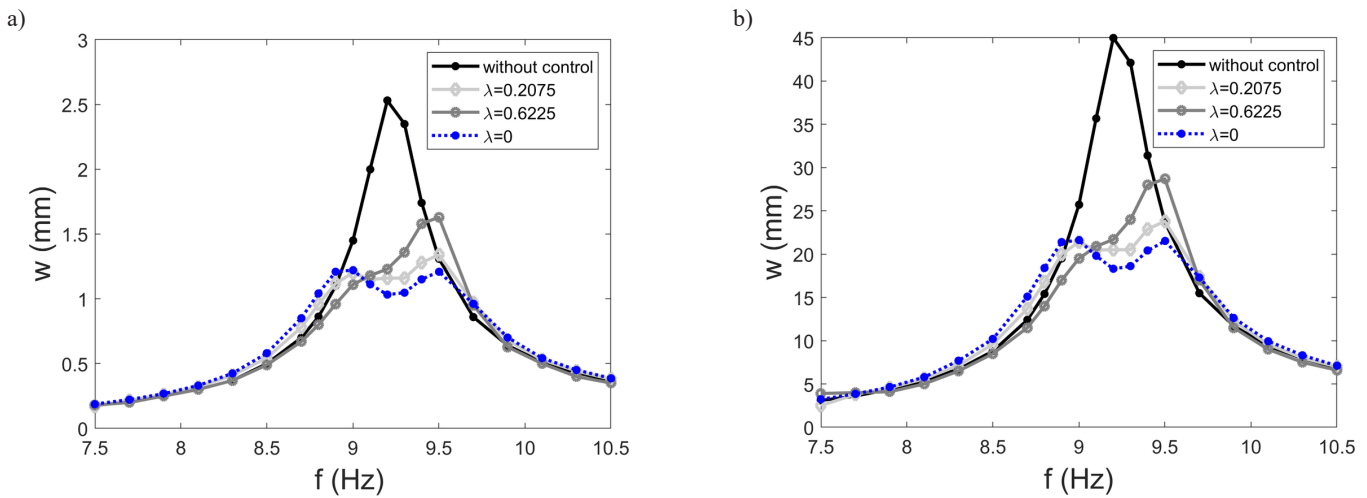

Fig. 9. Comparison of the resonance curves for a system without control and with the second variant of non-ideal control, and the results of: Abaqus sensor signal (a), free end response (b)
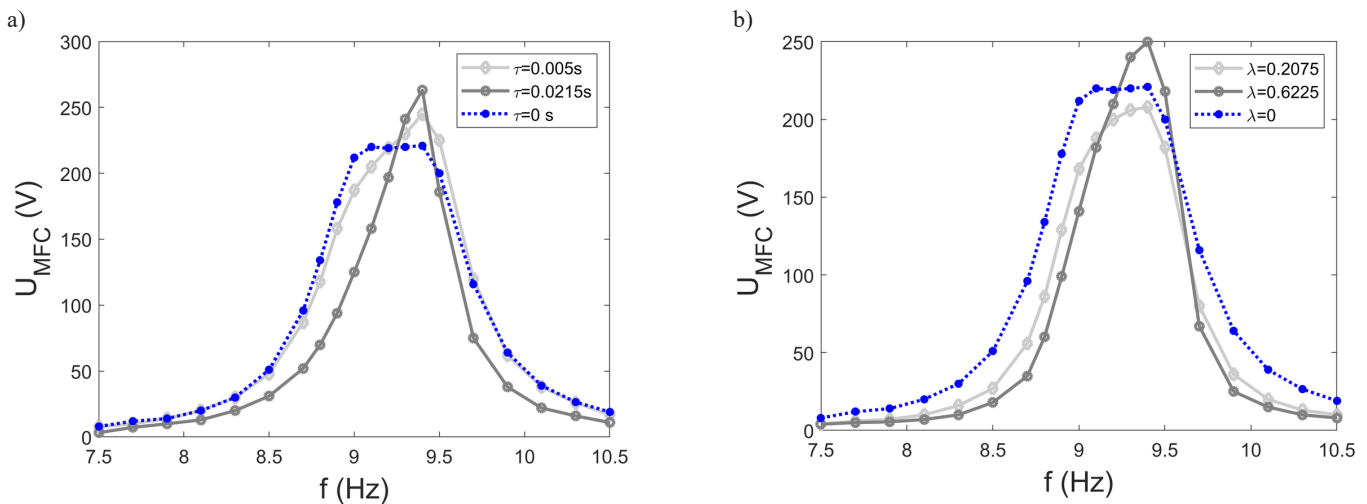

Fig. 10. Comparison of the curves showing the voltage supplied to the MFC actuator for the first variant of non-linear control (a) and the second variant of non-linear control (b)

i.e. the disappearance of the first resonance peak and the increase in the second one.

Interesting observations can be made regarding the voltage curves of the MFC actuator (Fig. 10). For the model with the first-order inertial term and $\tau > 0$ s, the maximum voltage values are similar (Fig. 10a), but the widths of the resonance peaks are visibly different. In Figure 10b these relationships are reversed. The widths of the peaks for $\lambda > 0$ are similar but their maximum amplitudes differ to a significant extent.

4. Experimental findings

In previous sections were presented the research object and its finite element model (Section 2) and numerical analysis results (Section 3). This section presents some experimental details and obtained experimental data which were used to verify the numerical results. To compare numerical and experimental results, both the numerical analysis and the experiment must be performed under the same conditions. This section describes two problems that occurred during the experiment and how they were resolved. One of the key elements of the test stand is a DSP controller (see Figure 1). Signals from the sensor and to the high voltage amplifier are analogue. However, operations performed by the processor are based on digital signals. Consequently, the conversion from analogue to digital signal, and vice versa, is necessary. The first problem occurred already at the stage of writing the code in the DSP controller. Generally, the DSP controller code was based on Equations 5a-k, but the value gains γ_1, γ_2 had to be appropriately recalculated. This was due to the fact that in the FE model, the γ_1 parameter also included the gain of the high voltage amplifier and the influence of the A/D and D/A converters had to be taken into account, too. In effect, the gains used in the DSP controller code were calculated from the following dependencies:

$$\gamma_1 = 50000\gamma_{A-D} \tag{10a}$$

$$\gamma_2 = \frac{1000\gamma_{D-A}}{200} \tag{10b}$$

where the values 50000, 1000, 200 are γ_1, γ_2 used in the FE model and high voltage amplifier gain, whereas γ_{A-D}, γ_{D-A} are the gains of the converters: from analogue to digital and from digital to analogue, respectively. The values of these gains depend on the type of applied converters. Based on the specifications of both converters, the values of γ_{A-D} and γ_{D-A} were assumed to be 0.00030525 and 6553, respectively. The controller configuration was checked for correct operation in two steps. An analysis of the controller equation (3) revealed that for the signals w_{sensor}=0 or w_{sensor}=0.1sin(58.12t), free or forced vibrations of a single linear oscillator should be obtained. The expected vibration amplitudes of such oscillator can easily be determined from the vibration theory for linear systems. In the first step, free vibration of the controller was observed. The following parameters were applied: γ_1=0 s^{-2} (instead of w_{sensor}=0), n=0 rad/s, $\omega_{control}$=58.12 rad/s, γ_2=5γ_{D-A}, and the controller initial conditions were $U_{control}$=0.1 V, $V_{control}$=0 V/s. For a well-selected parameter γ_{D-A} at the controller output (before the high voltage amplifier), free undamped vibration with an amplitude of 0.5 V should be observed. The parameters used in the second step were as follows: γ_1=500γ_{A-D}, γ_2=5γ_{D-A}, n=2 rad/s,

$\omega_{control}$=58.12 rad/s, w_{sensor}=0.1sin(58.12t) (signal from the signal generator), and the controller initial conditions were $U_{control}$=0 V, $V_{control}$=0 V/s. For this case, with a well-selected parameter γ_{A-D} forced vibration with an amplitude of about 1.0754 V should be observed. Results of both tests of the PPF controller are shown in Figure 11. In the first case (Fig. 11a), the controller response is in accordance with the assumptions, i.e. one can observe periodic oscillations with an amplitude of 0.5 V. In the other case, the obtained response is similar to the expected one (Fig. 11b). The small observed discrepancy may result from the precision of the applied signal generator. The experimental results confirm that the controller operates properly. The presented time series confirm that the gains γ_{A-D} and γ_{D-A} describing signal conversion must be taken into account, because it is the only way to obtain the desired controller response.

In the numerical tests, a relative displacement of the selected point (x=60 mm) was used for control, which we called an Abaqus sensor signal. The second problem in the experiments was related to direct determination of this relative displacement. The experimental setup consisted of three sensors: two accelerometers and one strain gauge. One accelerometer was fixed to the shaker armature to provide information about excitation. It was used for shaker control. The other accelerometer and the strain gauge were fixed to the beam at a distance of x=60 mm from the clamping. This location was the same as that of the Abaqus sensor signal. Both sensors measured the beam's response, with the accelerometer measuring absolute motion while the strain gauge measured relative motion. Double integration of the difference between signals from the accelerometers makes it possible to determine the amplitude of beam relative motion w_{sensor}. However, this approach is useless for real-time control. The use of the strain gauge as a controller input is more convenient. In this case, strain should be converted into displacement. The proposed simple conversion method involves comparing resonance curves from both beam sensors (strain gauge and accelerometer). Figure 12 shows the resonance characteristics for the system without control, where the beam vibration describes the deformation ε from the strain gauge (Fig. 12a) or relative displacement calculated from the accelerometer signals w_{sensor} (Fig. 12b). The black curves are similar, but the values of the vertical axis are approximately scaled by the constant $w_{sensor}/\varepsilon \approx 0.0075$ m/V. Finally, the signal from the strain gauge was used as a controller input (ε instead of w_{sensor}) in the controller efficiency tests. As a result, one of the controller gains (10a) had to include this change and thus be modified to the form:

$$\gamma_1 = 0.0075 \cdot 50000\gamma_{A-D} = 375\gamma_{A-D} \tag{11}$$

A new gain value γ_1 allows a proportional conversion of strain into data about displacement. Finally, the numerical and experimental re-
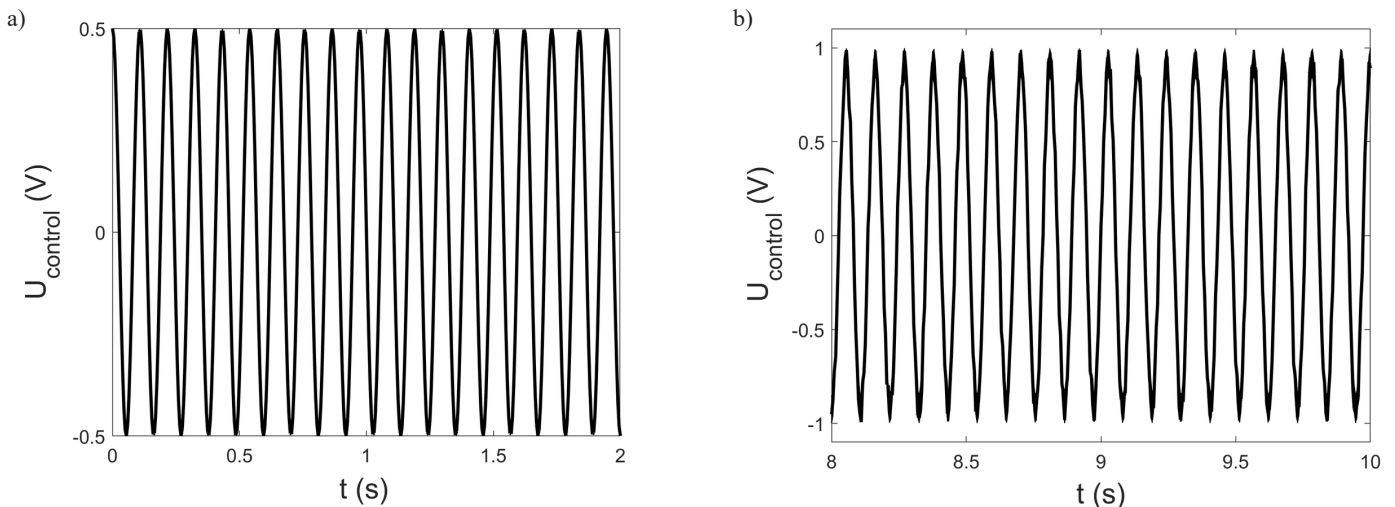
a)

b)

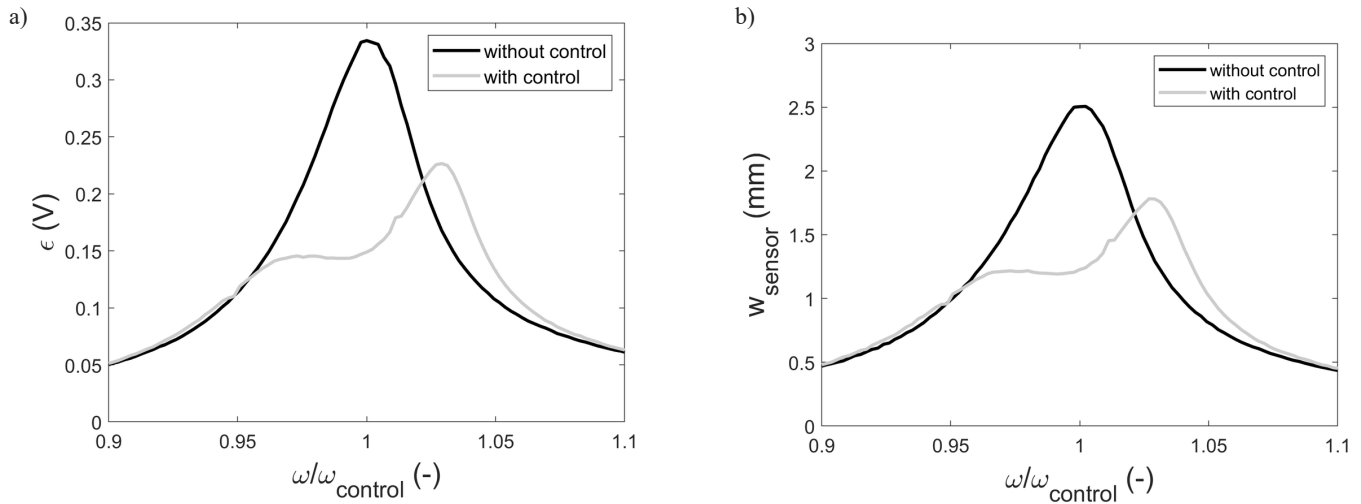Fig. 11. PPF controller tests. Obtained controller responses: free vibration (a) and forced vibration (b)

Fig. 12. Comparison of resonance curves obtained in the measurements made using: strain gauge ε (a) and accelerometers w_sensors (b)
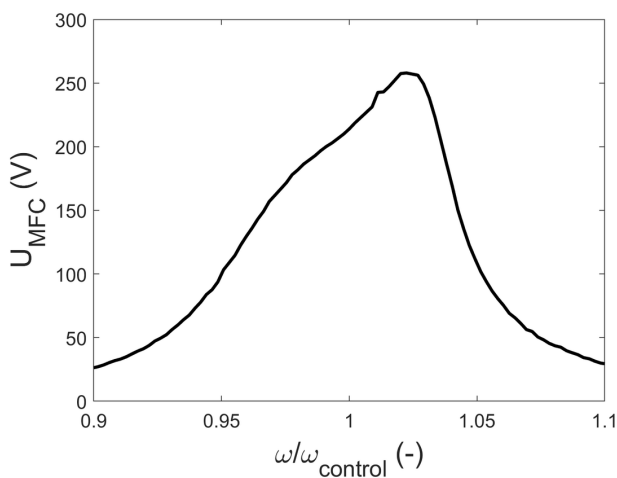

Fig. 13. Experimental resonance curves of voltage supplied to the MFC actuator

sults can be compared because the DSP controller calculations are based on the converted displacement.

Following the controller correction, dynamic tests with active control were performed. Figure 12 presents the comparison of experimental curves for a system with and without control.

The experimental characteristics (Figs. 12 and 13) were then compared with the numerical results: ideal control (Figs. 5a and 6), non-ideal control with the first order inertial term (Figs. 8a and 10a), and non-ideal control with Bouc-Wen hysteresis (Figs. 9a and 10b). The values of the characteristic points are listed in Table 1. Some important trends can be observed based on the data in this table. All curves have similar maximum amplitudes in the first resonance zone. At the dynamic elimination point, the vibration amplitudes are the same for ideal control and non-ideal control with a time constant. On the other hand, the amplitude for the model with Bouc-Wen hysteresis is closer to that obtained experimentally. As for the second resonance,

the vibration amplitude levels for systems with hysteresis are higher than for ideal control and are lower than the experimental data. The maximum voltages are different, too. The lowest value is obtained for the system with Bouc-Wen hysteresis. The maximum voltage yielded by the first hysteresis model ($\tau = 0.005$ s) is similar to that obtained experimentally.

All numerical conditions were reproduced in the experiments with due diligence. The experimental results confirm the existence of some discrepancies in relation to the model with ideal control. The numerical models with the proposed descriptions of the hysteresis effect make it possible to correct the responses obtained in order to make them closer to the experimental results. However, the comparison of the characteristics does not give a clear answer as to which hysteresis model describes the occurring phenomena better. Real objects can be characterized by additional factors which are not taken into account in numerical models, e.g. small time delays. This can render a complete fit of experimental and numerical data difficult, if not impossible.

5. Conclusions

Long-lasting vibrations are undesirable as they can affect rotor reliability. It is therefore of interest to investigate ways by which vibration could be reduced. A comparison of the curves with and without control reveals a significant vibration reduction after controller activation. It should minimize a negative vibration effect on the system's reliability. However, a large number of existing studies in the broader literature have only examined the problem of ideal control (without hysteresis, time delays, etc.). This paper described two variants of the hysteresis effect affecting the effectiveness of vibration control. The systems with ideal and non-ideal control were compared using the Abaqus software. The novelty of the finite element model developed in this study consisted of writing our own UAMP subroutine codes. The results demonstrated that hysteresis could reduce the PPF controller effectiveness. The use of this controller increased the number of resonance zones because it considered an additional equation of motion (3). The most significant negative changes were mainly related to the second resonance peak (Figs. 8-9). For larger values of

Table 1. Comparison of PPF control efficiency results from different numerical models and the experiment

Amplitude from resonance curve x=60 mm	Ideal control (3)	Non-ideal control (6) $\tau = 0.005$ s	Non-ideal control (7) $\lambda = 0.2075$	Experiment
First resonance peak (mm)	1.222	1.114	1.2	1.217
Dynamic vibration elimination $\omega/\omega_{control}=1$ (mm)	1.032	1.032	1.16	1.206
Second resonance peak (mm)	1.21	1.41	1.34	1.782
Maximum voltage (V)	220	245	208	257.9

the time constant τ or the parameter λ, a larger hysteresis loop was obtained but the controller effectiveness was reduced. Therefore, a larger hysteresis was found to be undesired. Although the vibration characteristics showed similar quality trends for both hysteresis variants under analysis, the obtained different shapes of voltage curves (Fig. 10) suggested different hysteresis mechanisms. Experimental tests were thus performed to investigate that problem. The experimental findings confirmed that the real system dynamics differed from the idealized case. The proposed inclusion of hysteresis enhanced the agreement between numerical and experimental results. The influence of hysteresis on the control efficiency was confirmed, but the study did not make it possible to unanimously determine which of the two descriptions was better to that end – the first order inertial term or the Bouc-Wen model. Based on the results, it can be concluded that the hysteresis effect should be taken into account when modelling piezoelectric actuators. In this study only one selected control method (PPF) was investigated. This research is planned to be continued because the knowledge about the sensitivity of different algorithms to hysteresis is of vital importance. Future research should investigate how hysteresis can change the effectiveness of various controllers and which of these controllers require hysteresis compensation.

References

1. Abaqus 6.14 documentation, <http://130.149.89.49:2080/v6.11/pdf_books/CAE.pdf> (08.04.2022).
2. Albaghdadi AM, Baharom M, Sulaiman S. Hybrid methodology using balancing optimization and vibration analysis to suppress vibrations in a double crank-rocker engine. Eksploatacja i Niezawodnosc – Maintenance and Reliability 2022; 24(1): 53-61, http://doi.org/10.17531/ein.2022.1.7.
3. Fenik S, Starek L. Optimal PPF controller for multimodal vibration suppression. Engineering Mechanics 2008; 15(3): 153-173.
4. Gan J, Zhang X. Nonlinear hysteresis modeling of piezoelectric actuators using a generalized Bou-Wen model. Micromachines 2019; 10(3): 1-12, https://doi.org/10.3390/mi10030183.
5. Gao JX, An ZW, Ma Q, Bai XZ. Residual strength assessment of wind turbine rotor blade composites under combined effects of natural aging and fatigue loads. Eksploatacja i Niezawodnosc – Maintenance and Reliability 2020; 22(4): 601–609, http://dx.doi.org/10.17531/ein.2020.4.3.
6. Gawryluk J, Mitura A, Teter A. Dynamic control of kinematically excited laminated, thin-walled beam using macro fibre composite actuator. Composite Structures 2020; 236(2): 1-7, https://doi.org/10.1016/j.compstruct.2020.111898.
7. Gawryluk J, Mitura A, Teter A. Dynamic response of a composite rotating at constant speed caused by harmonic excitation with MFC actuator. Composite Structures 2019; 210: 657-662, https://doi.org/10.1016/j.compstruct.2018.11.083.
8. Hamed YS, Kandil A, Machado JT. Utilizing Macro Fiber Composite to control rotating blade vibrations. Symmetry 2020; 12: 1-23, https://doi:10.3390/sym12121984.
9. Kedra R, Rucka M. Modelling of mechanical behaviour of high-frequency piezoelectric actuators using Bouc-Wen model. Metrology and measurement systems 2017; 24(2): 413-424, https://doi:10.1515/mms-2017-0022.
10. Kilikevicius A, Rimsa V, Rucki M. Investigation of influence of aircraft propeller modal parameters on small airplane performance. Eksploatacja i Niezawodnosc – Maintenance and Reliability 2020; 22(1): 1-5, http://dx.doi.org/10.17531/ein.2020.1.1.
11. Kwak MK, Heo S. Active vibration control of smart grid structure by multiinput and multioutput positive position feedback controller. Journal of Sound and Vibration 2007; 304: 230-245, https://doi.org/10.1016/j.jsv.2007.02.021.
12. Li CX, Li LL, Gu GY, Zhu LM. Modeling of rate-dependent hysteresis in piezoelectric actuators using a Hammerstein-like structure with a modified Bouc-Wen model. Intelligent robotics and applications 2016: 672–684, https://doi:10.1007/978-3-319-43506-0_58.
13. Liu Y, Shan J, Gabbert U, Qi N. Hysteresis and creep modeling and compensation for a piezoelectric actuator using a fractional-order Maxwell resistive capacitor approach. Smart Materials Structures 2013; 22(11): 1–12, https://doi.org/10.1088/0964-1726/22/11/115020.
14. Mitura A, Gawryluk J, Teter A. Numerical and experimental studies on the rotating rotor with three active composite blades. Eksploatacja i Niezawodnosc – Maintenance and Reliability 2017; 19(4): 571–579, http://dx.doi.org/10.17531/ein.2017.4.11.
15. Mitura A, Warminski J. Influence of piezoelectric actuator hysteresis on saturation control efficiency. Proceedings of the Institution of Mechanical Engineers. Part C: Journal of Mechanical Engineering Science 2020; 235(20): 4749-4759, https://doi.org/10.1177/0954406220946066.
16. Padoin E, Fonseca JSO, Perondi EA, Menuzii O. Optimal placement of piezoelectric macro fiber composite patches on composite plates for vibration suppression. Latin American Journal of Solids and Structures 2015; 12(5): 925-947, https://doi.org/10.1590/1679-78251320.
17. Panayotov F, Dobrev I, Massouh F, Todorov M. Experimental study of a helicopter rotor model in hover. Matec Web of Conferences 2018; 234: 1-5, https://doi.org/10.1051/matecconf/201823401002.
18. Parafiniak M, Skalski P. Vibration testing of a helicopter main rotor composite blade. Prace Instytutu Lotnictwa 2011; 218: 72-76.
19. Romanski L, Bieniek J, Komarnicki P, et al. Operational tests of a dual-rotor mini wind turbine, Eksploatacja i Niezawodnosc – Maintenance and Reliability 2016; 18(2): 201–209, http://dx.doi.org/10.17531/ein.2016.2.7.
20. Smart materials, <http://www.smart-material.com/MFC-product-mainV2.html> (08.04.2022).
21. Vadiraja DN, Sahasrabudhe AD. Vibration analysis and optimal control of rotating pre-twisted thin-walled beams using MFC actuators and sensors. Thin-Walled Structures 2009; 47(5): 555-567, https://doi.org/10.1016/j.tws.2008.10.004.
22. Wilbur ML, Wilkie K. Active-twist rotor control applications for UAVs. Transformational Science and Technology for the Current and Future Force. Proceedings of the 24th US Army Science Conference, 2006: 185-192.